Journal of Materials Chemistry B

Materials for biology and medicine

rsc.li/materials-b

ROYAL SOCIETY
OF CHEMISTRY
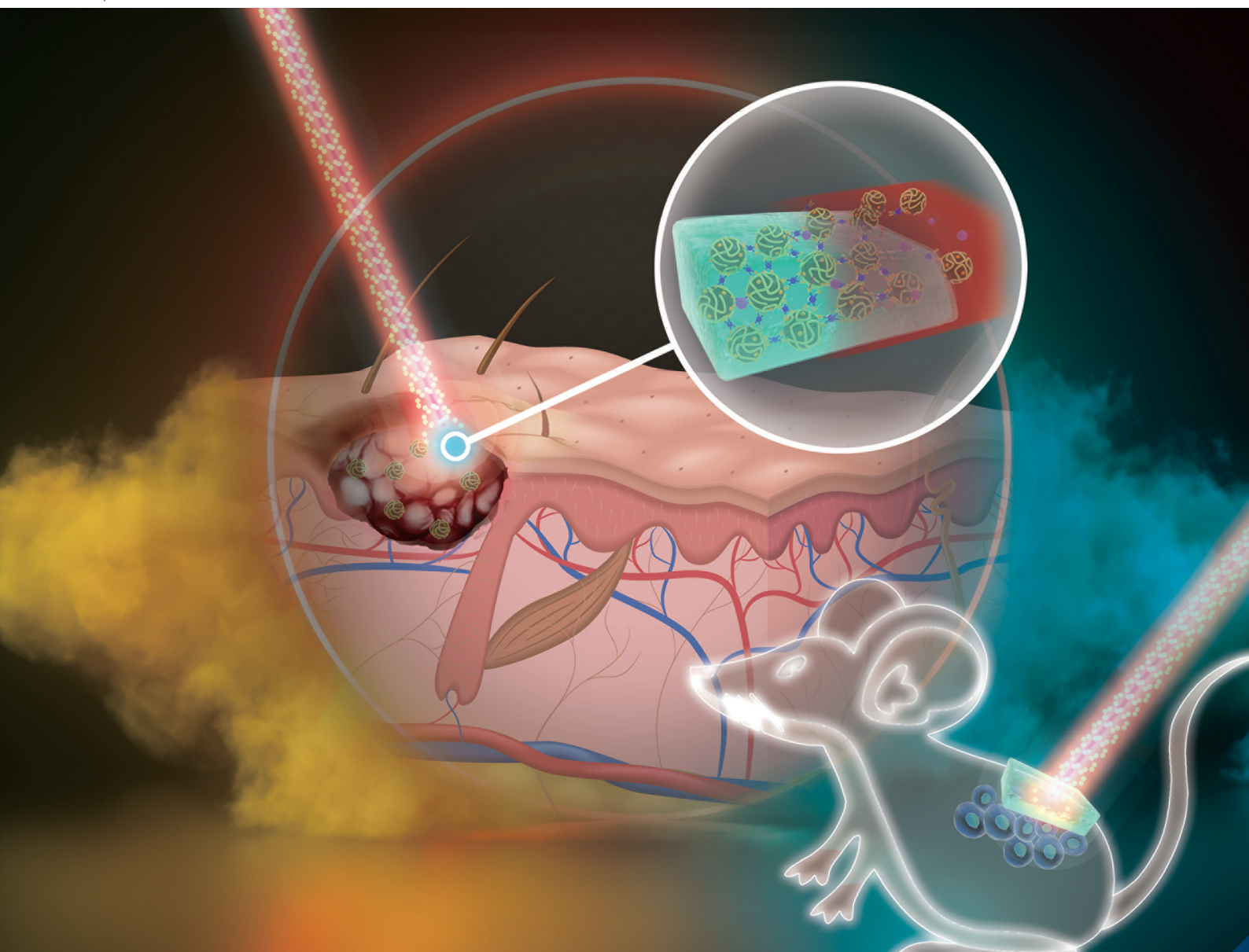
PAPER
Xiaolu Guo, Chanjuan Liu *et al.*
A NIR-II light-modulated injectable self-healing hydrogel for
synergistic photothermal/chemodynamic/chemo-therapy of
melanoma and wound healing promotion

Indexed in
Medline!

A NIR-II light-modulated injectable self-healing hydrogel for synergistic photothermal/chemodynamic/chemo-therapy of melanoma and wound healing promotion†

Xiaohua Huang,[a] Lei Tang,[a] Lin Xu,[a] Yu Zhang,[a] Guangyao Li,[a] Weiling Peng,[a] Xiaolu Guo,*[b] Li Zhou, [ID][a] Chanjuan Liu [ID]*[a] and Xing-Can Shen [ID][b]

The development of an injectable multifunctional hydrogel with tumor therapy, antibacterial treatment and wound healing properties is essential for simultaneously eradicating melanoma and promoting wound healing of tumor-initiated skin defects. Herein, iron ion-doped polyaniline (PANI(Fe)) tethered with guar gum (GG) chains is employed for the first time as a building unit for constructing a superior hydrogel (GG@PANI(Fe)-borax) crosslinked by borate/didiol bonds. Due to the dynamic and reversible properties of boronate ester bonds, the GG@PANI(Fe)-borax hydrogels had convenient injectability, rapid self-healing ability, and reversible gel–sol transformations under thermal- or pH-stimuli. More importantly, they took advantage of the second near-infrared (NIR-II) responsive photothermal conversion capability, accompanied by the photothermal-enhanced high cytotoxic •OH generation in the H_2O_2-enriched tumor microenvironment induced by iron-doped PANI. The as-prepared hydrogels exhibited excellent photothermal effects and controllable NIR-triggered drug release, leading to distinctly synergistic photothermal/chemodynamic/chemo-therapy effects of melanoma both *in vitro* (98.2%) and *in vivo* (98.8%). In addition, the obtained hydrogels also exhibited good anti-bacterial activity (>97.1%) against both Gram-positive (*Staphylococcus aureus*) and Gram-negative (*Escherichia coli*) bacteria because they were based on PANI(Fe) and borax, which exhibit antibacterial activity. Furthermore, these GG@PANI(Fe)-incorporated scaffolds could improve fibroblast cell proliferation and angiogenesis for accelerating wound repair in tumor-bearing and infected wound mice. Taken together, GG@PANI(Fe)-borax hydrogels may be used simultaneously for eradication of skin-tumor cells, inhibiting infection and accelerating wound healing. This work offers an effective and facile strategy to fabricate an "all-in-one" multifunctional hydrogel platform for synergetic multimodal integrated therapy of tumors.

Introduction

Melanoma is a highly aggressive cutaneous cancer with high rates of mortality.[1] Currently, widely applied traditional therapeutics such as surgery excision, chemotherapy and radiotherapy still suffer from several problems, including high risk of infection, severe adverse effects, undesirable drug resistance, great threat of recurring, and so on.[2–4] Photothermal therapy (PTT), a non-invasive treatment modality, utilizes photothermal agents to convert absorbed near-infrared (NIR) light into local hyperthermia for ablation of cancerous cells.[5–7] Benefiting from the high spatiotemporal accuracy of light, PTT minimized the adverse effects towards normal tissues and thereby exhibited significant advantages beyond conventional therapeutic modalities. In particular, the PTT mediated by the second near-infrared (NIR-II, known as the second biological window with a spectrum range of 900–1400 nm) has attracted great attention.[8–10] It has shown deeper tissue penetration and a higher laser tolerance threshold than the first near-infrared (NIR-I, 650–900 nm) due to the reduced light absorption and scattering. However, the extensively applied nanosized photothermal therapeutic agents *via* systematic administration suffer from uncontrollable distribution and poorly targeted delivery, which compromised the therapeutic effect.[11–13] Besides, treatment of melanoma involves not only the elimination of skin cancer cells, but also repairing tumor-initiated skin defects and avoiding bacterial invasion.[14–16]

[a] *Guangxi Key Laboratory of Optical and Electronic Materials and Devices, and College of Materials Science and Engineering, Guilin University of Technology, Guilin 541004, P. R. China. E-mail: liuchanjuan@glut.edu.cn*

[b] *State Key Laboratory for Chemistry and Molecular Engineering of Medicinal Resources, School of Chemistry and Pharmaceutical Science, Guangxi Normal University, Guilin, 541001, China. E-mail: guoxl@mailbox.gxnu.edu.cn*

† Electronic supplementary information (ESI) available. See DOI: https://doi.org/10.1039/d2tb00923d

This journal is © The Royal Society of Chemistry 2022

*J. Mater. Chem. B*, 2022, **10**, 7717–7731 | 7717

Therefore, the development of an effective localized PTT-based versatile platform for simultaneous elimination of melanoma, inhibiting wound infection, and promoting wound healing is urgently needed.

Hydrogels have been applied in the biomedical field for many years, including antitumor treatment,[17] wound management[18] and localized drug delivery.[19,20] The three-dimensional porous structures of hydrogels can easily encapsulate various therapeutic agents. Injectable hydrogels incorporated with therapeutic drugs can be precisely injected into targeted tumor locations using a syringe as long-acting drug storages for localized drug delivery, avoiding systemic drug side-effects in patients.[21,22] Meanwhile, hydrogels are promising wound dressings due to their hydrophilicity, soft-wet properties, and high porosity, which are similar to the extracellular matrix (ECM).[23] Hydrogel dressings provide a prolonged moist environment for optimizing gaseous exchange and nutrients supply to expedite wound healing. In particular, hydrogels with reversible cross-linked polymer networks based on dynamic covalent or reversible physical crosslinking tend to possess a self-healing capability,[24] which can provide better wound protection avoiding secondary injury or bacterial infection, especially for wounds on the stretchable parts of the body.[25] Recently, some injectable self-healing hydrogels that integrate multimodal anticancer, bacteria inhibition, and wound healing acceleration abilities have been developed.[14,26] Nevertheless, such multifunctional hydrogels are still limited by complicated constructions, and tedious integrations, thereby far from being safe and reliable enough for clinical applications.

Organic π-conjugated polymers, such as polyaniline (PANI),[27–29] polypyrrole (PPy),[30,31] polythiophene,[32] and their derivatives, as a novel generation of promising photothermal agents have attracted tremendous attention, and possess a strong absorption coefficient in the NIR window, high photothermal conversion efficiency, and superior photostability. Among them, polyaniline (PANI) is the first reported polymer-based photothermal agent for anticancer therapy. Meanwhile, PANI exhibits intrinsic antibacterial activity especially for Gram-positive bacteria,[33] and received special attention in PTT fields for both antitumor treatment and bacterial inhibition, because of its unique dope-able properties,[34] pH responsiveness[35] and facile synthesis. The NIR absorption and PTT effect of PANI could be significantly enhanced by the introduction of acidic groups or doping with metal ions into PANI chains, some of which enabled the tumor acidic microenvironment-activated PTT for selective ablation of cancer cells due to the pH-responsive conversion of emeraldine base (EB) to emeraldine salt (ES) of PANI.[36,37] In particular, PANI doped with transition metal ions not only increased the charge transfer rate to enhance the PTT effect,[38,39] but also the doped transition metal ions are expected to produce $\cdot OH$ for synergic killing of cancer cells by Fenton or Fenton-like reactions in the H_2O_2-enriched specific tumor microenvironment (TME). However, the studies of PANI-based photothermal agents were focused on the NIR-I region, and NIR-II-mediated PANI-based therapeutic agents are rarely reported.[40]

To overcome the above issues, we present here a facile method to construct an "all-in-one" multifunctional hydrogel platform without complicated integration to simultaneously combine PTT/CDT/chemotherapy synergic therapy and accelerate wound healing. This polymer network of superior hydrogel integrated with intrinsic features of NIR-II responsive photothermal characteristic, Fenton catalytic capability, antibacterial activity,
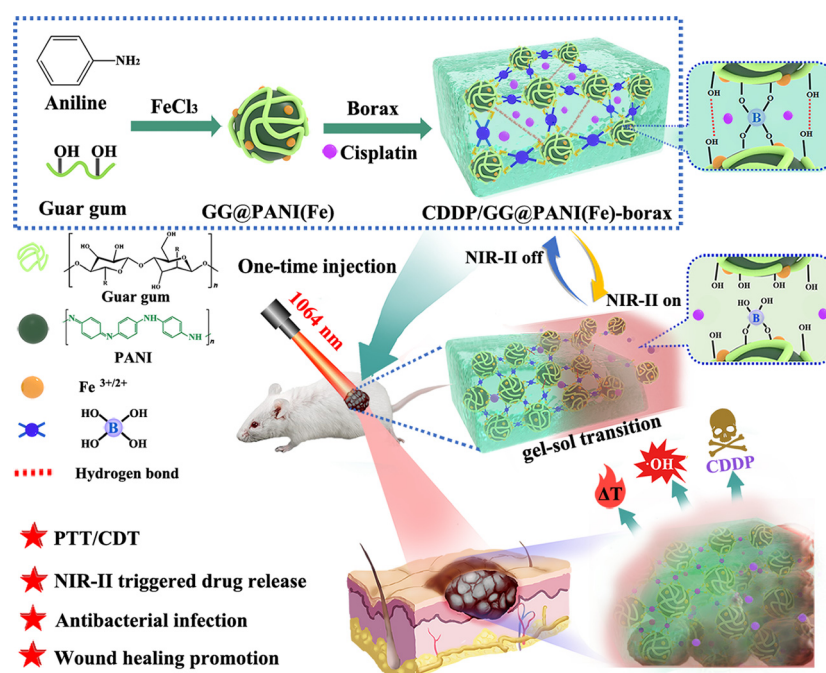
Scheme 1 Schematic illustration of the GG@PANI(Fe)-borax hydrogel based on dynamic covalent cross-linking applied for NIR-II modulated photothermal/chemodynamic and chemo-therapy of melanoma, antibacterial infection, and wound healing promotion.

7718 | *J. Mater. Chem. B*, 2022, **10**, 7717–7731

This journal is © The Royal Society of Chemistry 2022

and rapid self-healing properties in a single system. This novel hydrogel was simply prepared by utilizing a transition metal-doped conjugated polymer (iron ions-doped polyaniline, denoted as PANI(Fe)) tethered with naturally occurring polysaccharide (guar gum, denoted as GG) as building blocks and borax as a cross-linker with the help of dynamic covalent borax/ didiol linkages and hydrogen bonding (Scheme 1). Importantly, when PANI was doped with iron ions and entangled with GG, the absorption spectrum exhibited a significant red shift and had excellent NIR-II-responsive photothermal conversion, the iron ion-doped PANI not only tethered the GG chains to enable the hydrogel formation, but also served as the NIR-absorbing photothermal mediators and Fenton catalyst for synergic PTT/ CDT. Since borax/didiol cross linkages are dynamically reversible and multi-stimuli responsive,[41] the ultimate hydrogel (GG@PANI(Fe)-borax) exhibited an automatic self-healing capability and thermal-/pH- triggered gel–sol transformation. In addition, because polyaniline has antibacterial activity, especially against Gram-positive bacteria, and borax as a clinical traditional Chinese medicine widely used in ulcerative or infected wounds treatment.[42,43] Therefore, the as-prepared hydrogel had an excellent antimicrobial and wound management ability. As a result, the photothermal conversion efficiency of the GG@PANI(Fe)-borax hydrogel was calculated to be 44.81% under an NIR-II biological window (1064 nm laser). Consequently, the excellent therapeutic effect of eradication of most B16 melanomas was achieved through synergistic NIR-II modulated photothermal hyperthermia, TME-mediated high cytotoxic •OH production, and NIR-triggered on-demand *cis*-diamminedichloroplatinum (CDDP) release. In addition, GG@PANI(Fe)-borax was demonstrated to have an excellent contact anti-bacterial activity both *in vitro* and *in vivo*. Furthermore, the complete repair of the infected wound was achieved through treating by GG@PANI(Fe)-borax hydrogel for 12 days. To our knowledge, this is the first report of an NIR-II-modulated conjugated polymer-based self-healing hydrogel for simultaneous synergetic multimodal therapy, antibacterial infection, and adjuvant wound repair. This work provides an effective and facile strategy for the rational design of a new-generation NIR-II-responsive injectable self-healing hydrogel for multifunctional integrated therapy of tumors.

Experimental section

Synthesis of GG@PANI(Fe) composite and GG@PANI(Fe)-borax hydrogel

The water-soluble GG@PANI(Fe) composite were prepared by a one-step oxidative polymerization of aniline in the presence of FeCl$_3$ as both the oxidant and dopant, and GG as the stabilizer. Briefly, GG (100 mg) and aniline (93 μL) were completely dissolved in 10 mL of deionized water and stirred at room temperature for 30 minutes, then FeCl$_3$ (1.4 wt% in 70 mL aqueous solution) was added dropwise into the above mixture, and reacted for 8 h at 0–5 °C to form a dark-green solution. After that, the reaction was restored to room temperature and carried out for another 24 h. Eventually, the GG@PANI(Fe)

composite were obtained by centrifugation, elutriation with water and lyophilization. For control experiments, PANI(Fe) was synthesized using the same procedure in the absence of GG, and GG@PANI composite was obtained by utilizing APS (230 mg) instead of FeCl$_3$ as the oxidant under the same conditions.

Subsequently, the hydrogels were quickly formed by simply mixing GG@PANI(Fe) composite with borax. Generally, a predetermined concentration of GG@PANI(Fe) composite (10, 15, 20 mg mL^{-1}) in 1 mL aqueous solution was slowly added with 30 μL borax aqueous solution (10 mg mL^{-1}), the mixed solution was stirred uniformly and left at room temperature until a homogeneously stable hydrogel was formed. These formed hydrogels were denoted as G1, G2, and G3, respectively. For control experiments, GG-borax was prepared using GG solution and borax as raw materials. In order to obtain the drug-loaded hydrogel, CDDP was mixed with GG@PANI(Fe) composite in advance, then the same gelation procedure was performed to obtain the CDDP/GG@PANI(Fe)-borax hydrogel. The gelation time of the hydrogels was tested by an upside-down experiment. For all samples, make the mixture uniform and start calculating the gelation time, followed by slowly inverting the sample, until the sample solution in the glass bottle no longer flows as a judgment of hydrogel formation. In addition, the glass bottles containing GG@PANI(Fe)-borax hydrogel were put into a water bath at a specified temperature and heated for 15 minutes. After that, the gel–sol transition temperature ($T_{gel-sol}$) was determined by the same inversion method.

Measurements of photothermal performance

To investigate the photothermal conversion effect, 2 mL of borax solution (10 mg mL^{-1}), GG@PANI(Fe) (10 mg mL^{-1}), and GG@PANI(Fe)-borax hydrogel (G1) were put into a cuvette and irradiated with an 808 nm or 1064 nm laser with a power density of 0.5 W cm^{-2} for 10 minutes. The corresponding temperature and photothermal images were synchronously recorded with an Infrared camera (MAG30, Magnity Electronics, China) and analyzed using ThermoX software.

To evaluate the photothermal-sensitive gel–sol phase transition of the hydrogel under NIR laser irradiation, 0.5 mL of hydrogel in a vial were continuously irradiated by a 1064 nm laser at a power density of 0.5 W cm^{-2} for 30 min, and the as-generated sol was collected and weighed at pre-determined intervals.

Detection of the •OH generation of the GG@PANI(Fe)-borax

The •OH production was firstly evaluated using the colorimetric method with 3,3′,5,5′-tetramethylbenzidine (TMB) as the substrate. The GG@PANI(Fe)-borax hydrogel precursor was prepared by diluting 10 times using PBS buffer (pH = 7.4 and 6.5) before gelation. This was followed by successively adding H$_2$O$_2$ (500 μM) and TMB (1.6 mM), and the variety of absorbance spectra were recorded using an UV-vis-NIR spectrophotometer and monitored for 15 minutes.

Electron spin resonance spectroscopy (ESR) was used to further confirm the production of •OH by using 5,5-dimethyl-1-pyrroline *N*-oxide (DMPO) as a spin trap. H$_2$O$_2$ (10.0 μM) and

DMPO (6.0 mM) in 1.0 mL PBS buffer (pH = 6.5) was put into a dark Eppendorf tube in advance. Subsequently, the reaction groups were respectively mixed with 10 µL of the following additions: borax (0.3 mg mL^{-1}), GG (1.0 mg mL^{-1}), GG@PANI(Fe) (1.0 mg mL^{-1}), and GG@PANI(Fe)-borax precursor (diluted 10 times). After mixing for 1 minute, the above mixture solution was transferred to a quartz capillary to collect the ESR signal using a Bruker A300 spectrometer at room temperature.

The cell migration analysis

A scratch test was performed to determine the effect of hydrogel extracts on cell migration, where the hydrogel extracts were obtained through dialysis in DMEM for 24 h at 37 °C. L929 cells were seeded (1.0×10^4 cells per well) in 6-well plates ($n = 5$) and cultured for 24 h. Then the cells were scratched with a pipette tip in the middle of the well (200 µL) to mimic an incisional wound, and then the scratches were recorded immediately using an invert microscope. After that, fresh medium containing hydrogel extracts of GG@PANI-borax and GG@PANI(Fe)-borax were added to the well, respectively. the untreated group was used as the control. After incubating for another 6 h, the cell migration status around the scratched region was re-photographed again. The scratch wound area was analyzed using Image J software, and quantitatively calculated using the equation: Relative wound area (%) = $(A_0 - A_t)/A_0 \times 100\%$, ($A_0$: the initial scratch area and A_t: the final scratch area).

Skin tumor therapy *in vitro*

To evaluate the cell-killing efficacy of the hydrogel therapeutic platform for PTT, CDT, and chemotherapy against melanoma, skin cancer cells (B16, 1×10^4 cells per well) were seeded in 96-well plates and allowed to attach for 24 h. Afterward, the cells were treated for 6 h under different conditions: blank (treated with PBS), blank + laser, CDDP, CDDP + laser, GG@PANI(Fe)-borax, GG@PANI(Fe)-borax + laser, GG@PANI(Fe)-borax + H$_2$O$_2$ + pH 7.4, GG@PANI(Fe)-borax + H$_2$O$_2$ + pH 7.4 + laser, GG@PANI(Fe)-borax + H$_2$O$_2$ + pH 6.5, GG@PANI(Fe)-borax + H$_2$O$_2$ + pH 6.5 + laser, CDDP/GG@PANI(Fe)-borax + H$_2$O$_2$ + pH 6.5, CDDP/GG@PANI(Fe)-borax + H$_2$O$_2$ + pH 6.5 + laser, the concentration of H$_2$O$_2$ and CDDP were 200 µM and 5 µM, respectively. For laser treated groups, the cells were irradiated with a 1064 nm laser (0.5 W cm^{-2}) for 5 minutes after 6 h of co-incubation. Thereafter, the standard MTT assay and live/dead staining assay were performed to investigate the cell viability.

In vivo antitumor activity

All animal experimental procedures were performed according to the Guideline for animal experimentation approved by the animal ethics committee of Guangxi Normal University. The melanoma model was established by subcutaneous injection with 100 µL of a suspension of B16 cells (1×10^6 cells in PBS) in the right hand side of each Kunming mouse (female, 6-weeks old, obtained from Hunan SJA Laboratory Animal Co. Ltd). When the tumor size reached approximately 100–150 mm^3, a full-thickness circular skin incision (10 mm in diameter) was created at the tumor site, then the mice were randomly divided into 8 groups

($n = 3$), they were non-laser-treated groups including (i) saline, (ii) CDDP, (iii) GG@PANI(Fe)-borax, (iv) CDDP/GG@PANI(Fe)-borax, and laser-treated groups including (v) saline + laser, (vi) CDDP + laser, (vii) GG@PANI(Fe)-borax + laser, (viii) CDDP/GG@PANI(Fe)-borax + laser. Then these mice were treated with intratumoral injection of: (i and v) 100 µL of saline; (ii and vi) 100 µL of free CDDP solution by one-time injection (at doses of 4 mg kg^{-1} body weight); (iii and vii) 100 µL of GG@PANI(Fe)-borax (*via* a single injection); and (iv and viii) 100 µL of CDDP/GG@PANI(Fe)-borax (*via* a single injection, at doses of 4 mg CDDP per kg body weight), respectively. Thereafter, the mice in laser-treated groups were irradiated with a 1064 nm laser (0.15 W cm^{-2}) for a total of four cycles (10 minutes per cycle) on the 1st, 3rd, 5th, and 7th days post injection. Meanwhile, the tumor temperature and thermographic images were recorded by an infrared thermal camera. The tumor volume and body weight were monitored every day during the whole therapy period, and the volume was calculated as follows: tumor volume = $1/2 \times$ tumor length $\times$ tumor width^2. Mice were sacrificed after the administration of 14 days, and the tumors and major organs (including heart, liver, spleen, lung and kidney) were excised for histological analysis using haematoxylin–eosin (H&E) stains.

In vivo antibiotic activity and infected wound healing

The *in vivo* antibacterial activity and wound healing assay was conducted on a *S. aureus*-infected wound mouse model. Briefly, the infection wounds were established by creating full-thickness circular skin incisions (10 mm in diameter) on the backs of Kunming mice (6 weeks old) and inoculating *S. aureus* (1.5×10^6 CFU mL^{-1}, 50 µL) onto the wound. After that, the mice were randomly divided into four groups and the infected wounds were covered with *in situ* injection of 200 µL GG-borax, GG@PANI-borax and GG@PANI(Fe)-borax hydrogel, respectively. To monitor the wound healing process, the wound locations were photographed at day 1, 3, 6, 9, and 12 post treatment, and the wound areas were analyzed with ImageJ software. After 12 days of treatment, all mice were euthanized and the wound skin tissues were excised. To determine the bacteria number in the treated wound, half of the skin tissues were homogenized and diluted 10 times with PBS, then 100 µL of the diluted solution was spread evenly on the LB agar plate. After incubating at 37 °C for 24 h, the colonies formed were counted. The other half of wound tissues were fixed with 10% formalin and stained with H&E for histologic assessment. The wound closure rates were calculated as follows: wound healing rate = (wound area at day 0 − wound area at certain day)/wound area at day 0.

Results and discussion

Synthesis and characterization of GG@PANI(Fe)-borax

Prior to the hydrogel, the GG@PANI(Fe) composite was prepared by a one-pot oxidative polymerization of aniline with FeCl$_3$ as an oxidant in the presence of GG as the stabilizer (Fig. 1A and Fig. S1, ESI†). GG@PANI(Fe) composites with different GG/ANI feed weight proportions of 0/1, 0.5/1, 1.05/1,
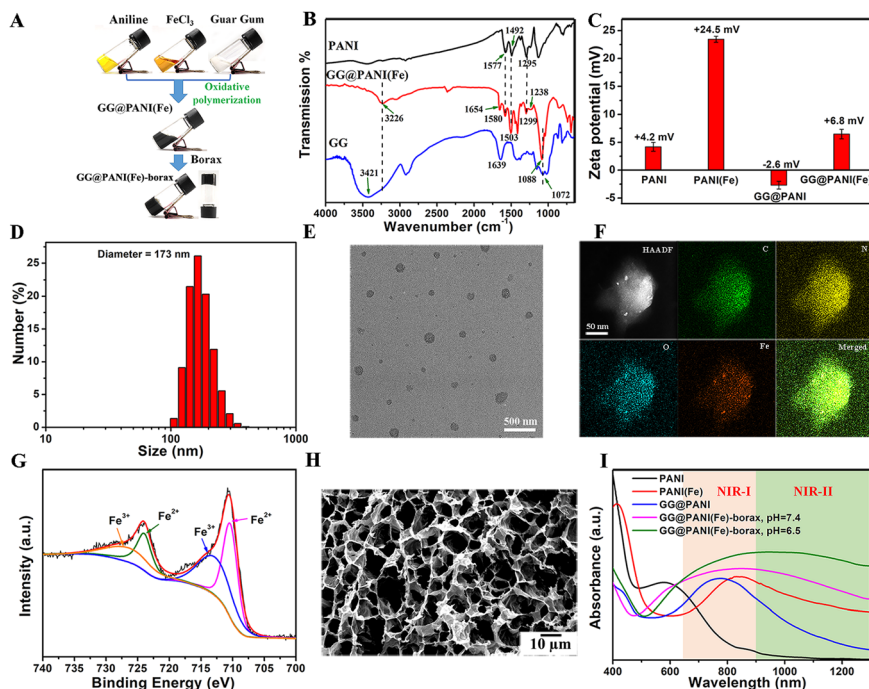
7720 | *J. Mater. Chem. B*, 2022, **10**, 7717–7731

This journal is © The Royal Society of Chemistry 2022

Fig. 1 Synthesis and characterization of GG@PANI(Fe)-borax. (A) Digital photos of the gelation process of GG@PANI(Fe)-borax. (B) FTIR spectrum of PANI, GG and GG@PANI(Fe). (C) Zeta potential of PANI, PANI(Fe), GG@PANI and GG@PANI(Fe) ($n = 3$). (D) DLS analysis for GG@PANI(Fe). (E) TEM image of GG@PANI(Fe). (F) HAADF-STEM image of GG@PANI(Fe) and the corresponding elemental mapping of C, N, O, and Fe. (G) Fe 2p XPS spectra of GG@PANI(Fe). (H) SEM image of the freeze-dried GG@PANI(Fe)-borax. (I) UV-Vis-NIR absorbance spectra of PANI, PANI(Fe), GG@PANI, and GG@PANI(Fe)-borax precursor (pH = 6.5 and 7.4).

and 1.5/1 were prepared, and the particle sizes and surface potentials were determined by dynamic light scattering (DLS). The results in Table S1 and Fig. S2 (ESI†) show that when the polymerization takes place in the absence of GG stabilizer (*i.e.* the feed ratio of GG/ANI is 0/1), the PANI(Fe) showed a relatively small size of 95 nm and its zeta potential was +24.5 mV, which was ascribed to the iron ion-enabled electrostatic repulsion can effectively prevent aggregation of PANI. When GG as the water-soluble steric stabilizer introduced into this polymerization reaction, the GG molecular chains were entangled on the surface of PANI, which not only provided the excellent aqueous dispersibility to PANI, but also offered the cross-linked groups for the following gelation. The size of the GG@PANI(Fe) composite increased from 123 nm to 485 nm as the GG/ANI feed weight ratio increased from 0.5/1 to 1.5/1. Increasing the GG proportion even further, to 2:1 proportion, the GG@PANI(Fe) composite cannot form any more, which may be due to the formation of a high viscosity GG solution that hindered the polymerization of aniline.[44] All the GG@PANI(Fe) water dispersible composites can stabilize for more than seven days without obvious precipitation and change in size (Fig. S3 and Table S1, ESI†). Furthermore, the morphology of the GG@PANI(Fe) composites has been found to be a spherical-like structure and the size increases as the GG proportion increases at a lower GG proportion (GG/ANI ratio below 1.05:1) (Fig. 1E and Fig. S4, ESI†), increasing the GG proportion to 1.5:1, which is evidence of the aggregation into large particles without a clearly distinguishable morphology. Taking into account the morphologies,

dispersity and gelation performance, the GG@PANI(Fe) prepared with the GG/ANI feed ratio of 1.05:1 was used for the following investigation.

The chemical structure of the GG@PANI(Fe) composite was confirmed by FT-IR spectra (Fig. 1B). As shown in the spectra of the GG@PANI(Fe) composite, the bands at 1580 cm^{-1} and 1503 cm^{-1} are attributed to the stretching vibration of the quinoid and benzenoid structure of PANI, and the peaks located at 1299 cm^{-1} and 1238 cm^{-1} are due to the C–N stretching vibration, and these absorptions were similar as that of original PANI polymer without the presence of GG.[45] Meanwhile, the peaks at 3421 cm^{-1}, 1639 cm^{-1} and 1072 cm^{-1} are due to the O–H stretching vibration, O–H deformation vibration and C–O–C stretching vibration of GG, respectively.[46] On the other hand, these bands shifted to 3226 cm^{-1}, 1654 cm^{-1} and 1088 cm^{-1} in the GG@PANI(Fe) composite. These observations indicated the intermolecular hydrogen bonding between GG and PANI in the GG@PANI(Fe) composite. Additionally, the potential value of PANI was electropositive (+4.2 mV) and the GG@PANI composite had a negative charge of −2.6 mV (Fig. 1C), the inversion of surface potential proved that besides hydrogen bonding, the GG chains were also wrapped on the surface of PANI through electrostatic interaction. Moreover, the potential of GG@PANI(Fe) was +6.8 mV, which may be due to the positive electricity of the doped iron ion.

The EDS mapping illustrated that C, N, O, and Fe elements were homogeneously distributed in the spherical-like structure (Fig. 1F), and the amount of Fe element was estimated to be

This journal is © The Royal Society of Chemistry 2022

J. Mater. Chem. B, 2022, **10**, 7717–7731 | **7721**

6.39% in the GG@PANI(Fe) composite from the EDS line profiles (Fig. S5, ESI†). In addition, the XPS spectrum in Fig. 1G demonstrated the existence of Fe^{3+} and Fe^{2+} in the GG@PANI(Fe) composite,[47,48] and the amount of Fe^{2+} was estimated to be 54.2%, which could facilitate the Fenton reaction in TME for CDT. The valence state of Fe in GG@PANI(Fe) was also evaluated by the o-phenanthroline detection assay (Fig. S6, ESI†). It is observed that after the addition of GG@PANI(Fe), the o-phenanthroline (phen) molecules formed deep orange $[Fe(phen)_3]^{2+}$ complexes with a distinct characteristic peak at 510 nm,[49] indicating the existence of Fe^{2+} ions in the GG@PANI(Fe) composite. Besides, according to the calculation by TG analysis (Fig. S7, ESI†), GG@PANI(Fe) composite was composed of 51% GG and 49% PANI(Fe). Owing to the surface attached GG steric stabilizer of the GG@PANI(Fe) composite, the GG@PANI(Fe) composite was highly dispersed and stable in various physiological solutions for as long as two weeks (Fig. S8, ESI†).

Subsequently, the GG@PANI(Fe)-borax hydrogel was facilely fabricated by mixing the GG@PANI(Fe) composite with borax aqueous solution (Fig. 1A). Borax as a crosslinker is a common clinic drug widely used for disinfection and antiseptic treatment of skin diseases,[51] which can crosslink GG@PANI(Fe) composite by forming borate/didiol dynamic covalent bonds between borax and diols of GG, thus forming a hydrogel network in water. Besides, the hydrogen bonding between GG chains as a reversible physical crosslinking further promoted the formation of hydrogel (Fig. S1, ESI†). The gelation performance was closely related to the GG proportion (Table S2, ESI†), at the lower GG feed proportion (0.5:1), the gelation time was more than 24 h, and the formed gel could only be stable in PBS for 2 h. With the increase of GG proportion, the gelation time dramatically shortened and the gel stability increased. When the GG proportion increased to 1.05:1, the gelation time was shortened to 1.88 minutes. Increasing the GG ratio even further to 1.5:1, the gel forms rapidly within 25 seconds and the formed gel could be stable in PBS for more than two weeks. It is speculated that increasing the proportion of guar gum could provide more crosslinking sites, thus increasing the crosslinking density, improving the gel performance and gel stability. As shown in Fig. S9 (ESI†), the long-term stability of the GG@PANI(Fe)-borax hydrogel (the GG@PANI(Fe) prepared with the GG/ANI feed ratio of 1.05:1) in medium (DMEM) and PBS with different pH values over two weeks, which ensured the effective repeated photothermal therapy. The microscopic morphology of the lyophilized hydrogels was investigated via SEM (Fig. 1H), and the GG@PANI(Fe)-borax hydrogel showed interconnected network-like macroporous structures, which not only allows drug loading for antitumor treatment but also facilitates the permeability for accelerating wound healing.

The borate/didiol bonds not only provide dynamic and reversible properties but also have multi-stimuli response. The GG@PANI(Fe)-borax has interesting thermal- and pH-responsive reversible gel–sol transition properties.[50] These prepared GG@PANI(Fe)-borax hydrogels with different GG@PANI(Fe) concentrations were heated at specific temperatures for

15 minutes, and the gel–sol phase transition of G1, G2 and G3 appeared at 48, 50 and 55 °C by the inverting-vial method, respectively (Fig. S10, ESI†). The converted sol was able to quickly return to the gel state during the cooling process even after three heating-cooling cycles (Fig. S11, ESI†). The reversible gel–sol transition property of GG@PANI(Fe)-borax hydrogel provided the potential for repeated controlled therapeutic agent release. The gel–sol transition temperature of G1 was further determined to be 46 °C by the rheological temperature sweep modal (Fig. S12, ESI†). This is suitable for photothermal-triggered drug release and synchronous PTT, thus G1 was chosen for further study. Besides, except for the thermo-stimuli responsive, the GG@PANI(Fe)-borax hydrogel can also respond to pH variation, and the hydrogel was disintegrated into sol when an acidic solution was added (pH < 5), while the hydrogel could regenerate after adding alkaline solution (pH > 9). This is attributed to the pH responsive dissociation and recombination of the reversible borate/didiol complexations (Fig. S13, ESI†). The multiple stimulus responses of the hydrogel were expected to achieve precise controllable drug release.

Photothermal performance

The strong absorption of NIR light is a prerequisite for PTT, and the UV-Vis-NIR absorption spectrum was obtained to probe the potential of the GG@PANI(Fe)-borax hydrogel for photothermal conversion. As seen in Fig. 1I, PANI displayed an absorption band at 583 nm, which is assigned to the charge transfer between the quinone and benzene rings. While the charge transfer band of PANI(Fe) was substantially redshifted from the visible to NIR-I region (absorption peak at 832 nm) due to the iron ion-doping enhanced electron-delivery efficiency between the quinoid and benzenoid rings.[29] Furthermore, the absorption spectra of the GG@PANI(Fe)-borax precursor covered both NIR-I and NIR-II regions, which is probably attributed to the combined effect of iron-doping and multiple hydrogen bonding between GG and PANI. More importantly, the absorption in the NIR-II biological window linearly enhanced with the decrease of pH value (Fig. S14, ESI†). The mass absorption coefficient of GG@PANI(Fe)-borax at 1064 nm was calculated to be 25.2 $L \cdot g^{-1}\,cm^{-1}$ at pH 6.5 and 23.4 $L \cdot g^{-1}\,cm^{-1}$ at pH 7.4, respectively. This pH-activated and acid-enhanced NIR-II absorption intensity is a benefit for specific PTT in a mild acidic tumor microenvironment (pH = 6.5).

In view of the strong NIR absorption, we further investigated the photothermal conversion performance using an 808 nm and 1064 nm laser. Under laser irradiation (0.5 W cm^{-2}) for 10 minutes, there was no noticeable temperature change in borax solution. In comparison, the temperature of GG@PANI(Fe) solution can elevate to 41.2 °C (808 nm laser) and 41.4 °C (1064 nm laser), respectively. Notably, the temperature increment in the GG@PANI(Fe)-borax hydrogel was more obvious and the photothermal effect concentrated at the laser irradiation area due to the lower thermal diffusion in solid gel. The ultimate temperature rose to 51.2 °C (808 nm laser) and 51.4 °C (1064 nm laser), respectively (Fig. 2A and B). These temperatures were sufficient to ablate tumor cells and trigger the gel–sol
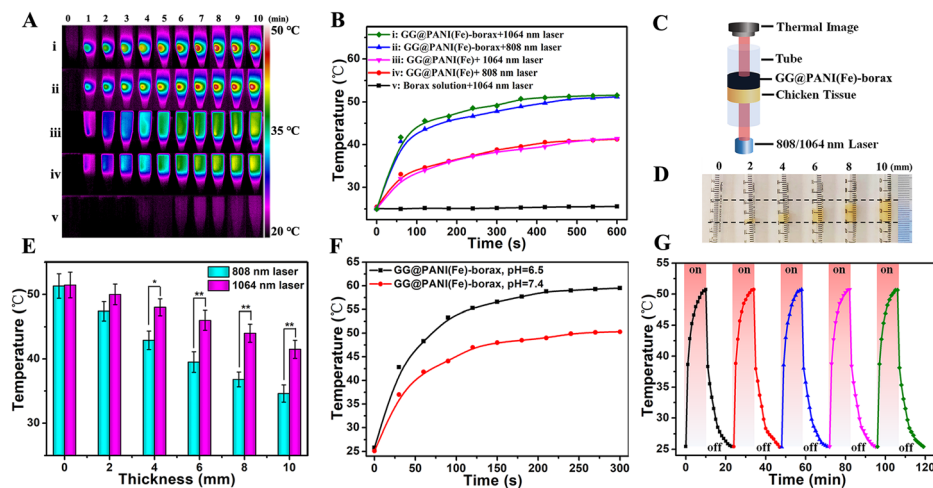
Fig. 2 Photothermal performance and tissue-penetration capability. (A) Thermo-graphic images of borax, GG@PANI(Fe), and GG@PANI(Fe)-borax hydrogel upon exposure to an NIR laser (10 min, 0.5 W cm^{-2}), and (B) the corresponding temperature evolutions with 808 nm and 1064 nm laser irradiation. (C) Schematic diagram for investigating the tissue-penetration capability of the NIR laser. (D) Different thicknesses of chicken breast tissues filled in transparent pipes were used as model biological tissues. (E) Temperatures of GG@PANI(Fe)-borax exposed to tissue-penetrating NIR-I (808 nm) and NIR-II (1064 nm) lasers (0.5 W cm^{-2}, *$P < 0.5$, **$P < 0.01$). (F) Changes of temperature with irradiation time for the GG@PANI(Fe)-borax hydrogel under 1064 nm laser irradiation (0.5 W cm^{-2}) at pH 6.5 and pH 7.4, respectively. (G) Temperature profiles of GG@PANI(Fe)-borax for five successive cycles of 1064 nm laser on (10 min, 0.5 W cm^{-2}) and off processes.

transition for drug release. Furthermore, the NIR-II biological window (900–1400 nm) is known to have a better tissue-penetration ability than the commonly utilized NIR-I window (650–900 nm), thus usually giving rise to a better deep-tissue photothermal effect.[52] To prove this concept, chicken breast tissues with different thicknesses were applied as model biological tissues to evaluate the deep-tissue photothermal conversion capability in both NIR-I and NIR-II windows (Fig. 2C and D). Owing to the scattering and absorption of light by the tissues, the temperature increments of the hydrogel exposed to tissue-penetrating NIR-I (808 nm) and NIR-II (1064 nm) lasers both gradually decreased as the tissue thickness increased (Fig. 2E). Nevertheless, the temperature elevations of hydrogel under the 1064 nm laser were always higher than those under the 808 nm laser. With the increase of tissue depth, the attenuation rate of temperature elevation with 1064 nm laser was obviously slower than that with the 808 nm laser (Fig. S15, ESI†), indicating the better tissue penetration capability in the NIR-II windows. Considering the advantage of the better tissue penetration capability and the higher maximum permissible exposure (MPE), the 1064 nm laser was chosen as the irradiation light for the subsequent *in vitro* and *in vivo* investigations.

Moreover, since the NIR absorption intensity of the GG@PANI(Fe)-borax hydrogel is pH dependent, we further investigated the photothermal effect at pH 6.5 and pH 7.4. As shown in Fig. 2F, the elevated temperature at pH 6.5 was 8.2 °C higher than that at pH 7.4 after 10 minutes irradiation with a 1064 nm laser. This differential temperature increment was conducive to selectively killing cancerous cells in the tumor microenvironment (pH = 6.5), while avoiding damage to the surrounding healthy tissues. Besides, the photothermal performance of the GG@PANI(Fe)-borax hydrogel was maintained at a constant during 5 consecutive cycles of laser on and off (Fig. 2G and Fig. S16, ESI†),

indicating its excellent photothermal stability for repeated photothermal treatment. The resultant photothermal conversion efficiency of GG@PANI(Fe)-borax was calculated to be 44.81% (1064 nm laser) (Fig. S17, ESI†).

•OH generation ability

Subsequently, the hydroxyl radical (•OH) production ability of GG@PANI(Fe)-borax was investigated using a colorimetric method with TMB as the substrate. A colorless TMB detection agent could be oxidized by •OH to yield blue (yellow) oxidized TMB (*ox*TMB) with a characteristic absorption peak at 652 nm (Fig. 3A). The UV-vis spectrum in Fig. 3B and Fig. S18 (ESI†) revealed that GG@PANI(Fe) composites and GG@PANI(Fe)-borax precursor (with or without TMB) did not have an obvious characteristic absorbance peak at 652 nm, and the absorption value at 652 nm did not change after adding H_2O_2 under pH 7.4 (simulated normal physiological environment), even with the H_2O_2 concentration up to 1.0 mM. In comparison, an obvious absorbance peak at 652 nm was observed under pH = 6.5 (simulated weakly acidic TME), the characteristic peak gradually enhanced as the increase of H_2O_2 concentration, confirming that the •OH could be effectively generated by GG@PANI(Fe)-borax under simulated weakly acidic TME, and this is based on the iron ion-based Fenton reaction converting H_2O_2 to •OH under pH 6.5. More importantly, the characteristic absorption intensity at 652 nm can be remarkably enhanced by 1064 nm laser irradiation, indicating the photothermal hyperthermia could significantly promote the Fenton catalytic activity and produce more •OH, which is helpful to achieve synergistic enhanced PTT/CDT effects. In addition, methylene blue (MB) is a dye that can be degraded by •OH, and as shown in Fig. S19 (ESI†), the absorption peak intensity of MB decreased with the degradation of MB when it was treated with GG@PANI(Fe)-borax precursor in
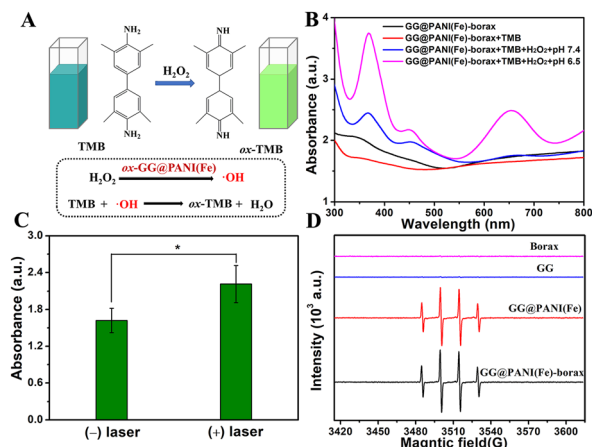
This journal is © The Royal Society of Chemistry 2022

J. Mater. Chem. B, 2022, **10**, 7717–7731 | **7723**

Fig. 3 Fenton catalytic activity and •OH production ability. (A) Schematic illustration of the TMB method to test the production of •OH by the Fenton reaction. (B) UV-vis spectra of GG@PANI(Fe)-borax (precursor), GG@PA-NI(Fe)-borax (precursor) + TMB, GG@PANI(Fe)-borax (precursor) + TMB + H_2O_2 + pH 7.4 and GG@PANI(Fe)-borax (precursor) + TMB + H_2O_2 + pH 6.5 (reaction for 15 minutes). (C) The absorption at 652 nm in the GG@PANI(Fe)-borax (precursor) + TMB + H_2O_2 + pH 6.5 group with or without 1064 nm laser irradiation (0.5 W cm^{-2}, 5 minutes) at the same reaction time of 15 minutes (*$P < 0.5$). (D) ESR spectra showing the generation of •OH by GG@PANI(Fe)-borax precursor in the presence of DMPO and H_2O_2 at pH 6.5.

the simulated TME (pH = 6.5, in the presence of H_2O_2). Nonetheless, when dimethyl sulfoxide (DMSO) as a •OH scavenger was added, the attenuation of the peak intensity for MB was negligible compared with that without DMSO. This result further confirmed the generation of •OH under TME. Moreover, ESR spectroscopy was also used to evaluate the •OH generation (Fig. 3D). As expected, the ESR signal of the GG@PANI(Fe)-borax precursor in the presence of trace H_2O_2 (approximated 10.0 μM) under pH 6.5 exhibited the characteristic •OH signal of four peaks, with the relative intensity ratio of $1 : 2 : 2 : 1$, demonstrating efficient generation of •OH. The above results revealed that the hydrogel containing iron ions is capable of Fenton reactions under the H_2O_2-riched TME and thus has the potential for effective CDT.

Self-healing and injectable ability

Due to the dynamic reversible property of the borate/didiol crosslinking and hydrogen bonding that drives the formation of GG@PANI(Fe)-borax, the resultant hydrogel exhibited an excellent self-healing capability. As shown in Fig. 4A, when three pieces of hydrogels including GG@PANI(Fe)-borax (black), GG-borax (clear) and rhodamine-stained GG-borax (red) were combined into a single piece of gel, it could be stretched up to approximately 300% strain after 2 minutes of self-healing. Thereafter, the combined gel was separated into the original three pieces following recombination color by color, then the damaged pieces adhered and autonomously healed to one integral gel again without external stimulus. During the self-healing process, the contact interface between the gels became blurred and the interconnecting region

became continuous, indicating that the two pieces of the gel became an integrated one (Fig. 4B). More remarkably, the self-healing capability of the GG@PANI(Fe)-borax hydrogel can also be achieved in PBS buffer (Fig. S20, ESI†). This facilitated its application for wound healing in a practical physiological microenvironment.

Besides, the self-healing performance of the GG@PANI(Fe)-borax hydrogel was also evaluated by rheological measurement. Amplitude oscillation was operated by continuously alternating the strain values at 5% and 500% (Fig. 4C). Under small strains, the storage modulus G' was greater than the loss modulus G'' behaving like an elastic solid, indicating the gel state. While under large strains, the G' became lower than G'' behaving like a viscous fluid, revealing the inner network was destroyed and the gel was liquefied, and when returning to the small strain again, the gel was reconstructed and rapidly recovered to the initial moduli. The recovery behavior was reproducible for multiple cycles without any distinct degradation, demonstrating the excellent self-healing property.

As a result of the dynamic reversible bonding structure, the gel was capable of shear-induced flow and instant recovery, and the viscosity of the GG@PANI(Fe)-borax hydrogel dramatically decreased with an increase of shear rate from 0.1 to 100 s^{-1} (Fig. 4D). This shear-thinning behavior endowed the gel with the potential for injectability, as observed in the illustration of Fig. 4D, and the GG@PANI(Fe)-borax hydrogel can be easily extruded through the 21-G needle to form the specific letters of
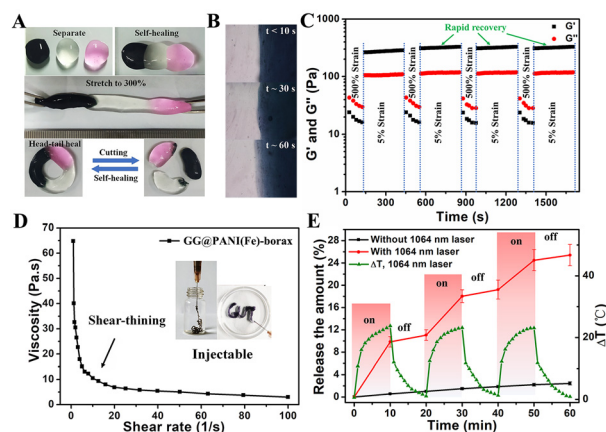

Fig. 4 Self-healing, injectable and controlled release drug capability of the GG@PANI(Fe)-borax hydrogel. (A) Three pieces of hydrogels (including GG@PANI(Fe)-borax (black), GG-borax (clear) and rhodamine-stained GG-borax (red)) could adhere to each other and instantly combined into a single piece, which could be stretched up to 300% strain. When the combined gel was separated into the original three pieces it can autonomously heal again within 2 minutes. (B) Optical microscopy images showing the changes of the interconnected zone between the GG-borax and GG@PANI(Fe)-borax over time. (C) Step-strain sweep of GG@PA-NI(Fe)-borax with an amplitude loop between small strain (5%) and large strain (500%). (D) The shear-dependent viscosity of the GG@PANI(Fe)-borax. The illustration is the injectable photographs. (E) Release of CDDP from the GG@PANI(Fe)-borax hydrogel under periodic irradiation (1064 nm laser, 0.5 W cm^{-2}) and the corresponding photothermal-induced temperature increase.

7724 | *J. Mater. Chem. B*, 2022, **10**, 7717–7731

This journal is © The Royal Society of Chemistry 2022

"GUT". In addition, the gel showed self-adaption to the irregular shapes. When the GG@PANI(Fe)-borax hydrogel was placed on the surface of a mold with irregular gaps, the gel gradually moved to completely fill the narrow gap spaces by gravity alone (Fig. S21, ESI†), demonstrating its satisfied self-adaption potential for irregular wounds, which could be attributed to the mobility of the polymeric network. Moreover, the hydrogel can tightly adhere to a finger and withstand the deformations caused by skin movement without falling off while maintaining its integrity, indicating the good adhesion and stretchability of the GG@PANI(Fe)-borax hydrogel (Fig. S22, ESI†). Taked together, the GG@PANI(Fe)-borax hydrogel with its suitable injectability, satisfied self-adaption, automatic self-healing ability, desirable adhesion and ductility, make it an excellent candidate for succedent melanoma therapy and wound healing.

NIR-triggered drug release *in vitro*

The excellent photothermal effects and thermo-sensitive gel–sol transition of the as-prepared hydrogel encouraged us to further explore its potential application for NIR-triggered therapeutic drug release. As shown in Fig. S23 (ESI†), the gel gradually transformed into a flowable sol phase under the continuous irradiation of a 1064 nm laser, demonstrating that the gel can efficiently convert low-dose NIR light to sufficient localized hyperthermia not only for PTT but also for promising controllable drug release *via* NIR-induced gel–sol transition. Hence, a water-soluble chemotherapeutic model drug CDDP was loaded into the gel to investigate the NIR-triggered drug release (Fig. S24, ESI†). The *in vitro* release profiles of CDDP from the hydrogel with pulsed laser irradiation (1064 nm, 0.5 W cm^{-2}) were investigated (Fig. 4E). As expected, over 9.8% of CDDP was released from the CDDP/GG@PANI(Fe)-borax hydrogel during the first cycle of laser irradiation for 10 minutes. When the laser was switched off, the release rate become considerably slower. During the second cycle of 1064 nm laser exposure, the release amount of CDDP was increased from 11.2% to 17.8% within 10 minutes. After three switch on/off irradiation cycles, the total release of CDDP was 25.4%. Whereas only 2.4% of the loaded CDDP was released within 60 minutes in the control group without laser exposure. This on-demand release characteristic was attributed to the acceleration of CDDP diffusion caused by the NIR-triggered gel–sol transition. Besides, the long-term release of CDDP from the GG@PANI(Fe)-borax hydrogel without NIR irradiation indicated that the hydrogel used as a drug depot can realize effective enduring therapy (Fig. S25, ESI†).

In vitro biocompatibility and anticancer efficiency

The biocompatibility of hydrogels is an essential prerequisite for their biomedical applications. The cytotoxicity of the obtained hydrogel was evaluated on L929 fibroblasts. As shown in Fig. 5A, L929 cells exhibited normal proliferation and the cell viabilities in all groups were higher than 95% after co-incubating with GG-borax, GG@PANI-borax, and GG@PANI(Fe)-borax hydrogels for 12 h, respectively, and the live/dead staining assay indicated that almost all the cells exhibited green fluorescence (representing live cells) (Fig. 5B). The above results demonstrated the excellent cytocompatibility. In addition, the hemolysis ratios in all the hydrogel groups (including GG-borax, GG@PANI-borax, and GG@PANI(Fe)-borax) were proved to be lower than the critical value of approved hemolysis (5%), verifying the satisfied hemocompatibility of the prepared hydrogel (Fig. 5C).

It was reported that iron ions were bioactive and could promote cell migration and differentiation, so as to accelerate wound healing.[53] Therefore, the effect of GG@PANI(Fe)-borax hydrogel extracts on the migration of fibroblast cells (L929) was evaluated by scratch wound healing assay. As shown in Fig. 5D and E, the scratch wound area in the GG@PANI-borax hydrogel
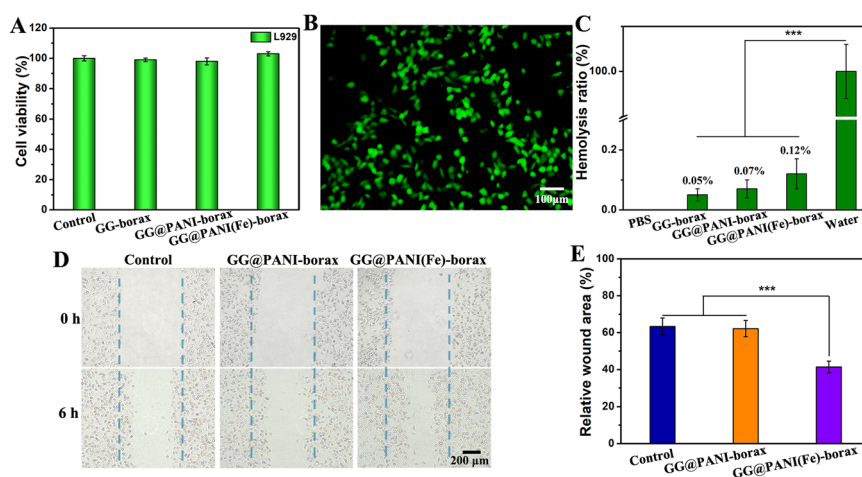

Fig. 5 *In vitro* biocompatibility and scratch wound assay. (A) Relative cell viability (L929 cells) after being co-incubated with GG-borax, GG@PANI-borax, and GG@PANI(Fe)-borax hydrogel for 12 h, respectively. (B) The corresponding fluorescent microscope images of Calcein AM/PI co-stained L929 cells in the GG@PANI(Fe)-borax hydrogel group. (C) The hemolysis rates of GG-borax, GG@PANI-borax, and GG@PANI(Fe)-borax hydrogel. (D) Microscope images of the migration state of L929 cells at 0 h and 6 h post scratching in the control, GG@PANI-borax, and GG@PANI(Fe)-borax group, respectively. (E) Relative wound areas of L929 cells in the control, GG@PANI-borax, and GG@PANI(Fe)-borax group after 6 h scratching. ***$P < 0.001$.

This journal is © The Royal Society of Chemistry 2022

J. Mater. Chem. B, 2022, **10**, 7717–7731 | **7725**

group (without iron ion doping) was close to the untreated control group after co-incubation for 6 h, and their relative wound areas were determined to be 62.2% (GG@PANI-borax hydrogel) and 63.4% (control group), respectively. Compared with the above two groups, the wound area in the GG@PA-NI(Fe)-borax hydrogel group (with iron doping) was obviously reduced, and the calculated relative wound area was 41.4%. This result revealed that iron ions played an important role in promoting the migration of fibroblast cells, and the GG@PA-NI(Fe)-borax hydrogel has the potential to accelerate the wound healing process *in vivo*.

In vitro anticancer efficiency

The intracellular reactive oxygen species (ROS) production by GG@PANI(Fe)-borax-mediated Fenton reaction was evaluated by using DCFH-DA as a fluorescent probe. As observed in Fig. 6A, almost no green fluorescence was observed in B16 cells treated with GG@PANI(Fe)-borax in the presence of H_2O_2 under pH 7.4. However, obvious green fluorescence was found as the pH value decreased to 6.5 in the GG@PANI(Fe)-borax group + H_2O_2 group, indicating the generation of $^{\bullet}OH$ radicals in a weakly acid environment. Notably, the fluorescence intensity increased after the introduction of 1064 nm laser irradiation, which demonstrated that hyperthermia induced by laser irradiation could enhance the production of $^{\bullet}OH$ in B16 cells.

Subsequently, the cell-killing efficiency of the GG@PANI(Fe)-borax hydrogel as a therapeutic platform for PTT, CDT and chemotherapy was evaluated. The cell viability and live/dead stained assay of B16 cells treated with different formulas are displayed in Fig. 6B and 6C, respectively. The PTT effect of the GG@PANI(Fe)-borax hydrogel was firstly evaluated. The B16 cells that received 1064 nm laser irradiation in the absence of H_2O_2 (GG@PANI(Fe)-borax + laser group) displayed significant

cell-killing efficiency and abundant dead cells with a low survival rate of 33.9%, suggesting the efficient PTT effect of the GG@PANI(Fe)-borax hydrogel *in vitro*. At the same time, for the cells containing H_2O_2 and without 1064 nm laser treatment, GG@PANI(Fe)-borax also show slightly tumor cell inhibitory effects at pH 6.5 with a cell viability of 81.2%, which could be attributed to the production of cytotoxic $^{\bullet}OH$ by GG@PANI(Fe)-borax-mediated Fenton reaction in a slightly acidic environment. In comparison, the cells treated with GG@PANI(Fe)-borax + H_2O_2 + pH 6.5 + laser showed higher cytotoxicity and relatively rare live cells with a low survival rate of 12.8%, revealing that the killing effect of PTT combined with $^{\bullet}OH$-mediated CDT was obviously stronger than the single CDT and single PTT. Notably, the cell survival rate in the CDDP/GG@PANI(Fe)-borax + H_2O_2 + pH 6.5 + laser group was reduced to the lowest (1.8%), and all of the cells displayed red fluorescence of dead cells, while the cell survival rate of the free CDDP group and CDDP + laser group at the same concentration were 73.9% and 70.6%, respectively. This excellent cell-killing effect of the CDDP/GG@PANI(Fe)-borax + H_2O_2 + pH 6.5 + laser group was because the hyperthermia not only mediated PTT but also enhanced the $^{\bullet}OH$ generation and CDDP release, resulting in the extremely low cell survival rate.

In vivo anticancer efficiency

Inspired by the excellent *in vitro* anticancer efficacy, we next explored the *in vivo* therapeutic efficacy of this versatile hydrogel for combined PTT-CDT and chemotherapy. B16 tumor-bearing mice were randomly divided into eight groups and treated with different administrations (Saline, free CDDP, GG@PANI(Fe)-borax and CDDP/GG@PANI(Fe)-borax, followed with or without laser irradiation for four cycles) (Fig. 7A). Upon the NIR-II laser irradiation at a low power density of 0.15 W cm^{-2} for 10 minutes, the mice treated with photothermal hydrogels (GG@PANI(Fe)-
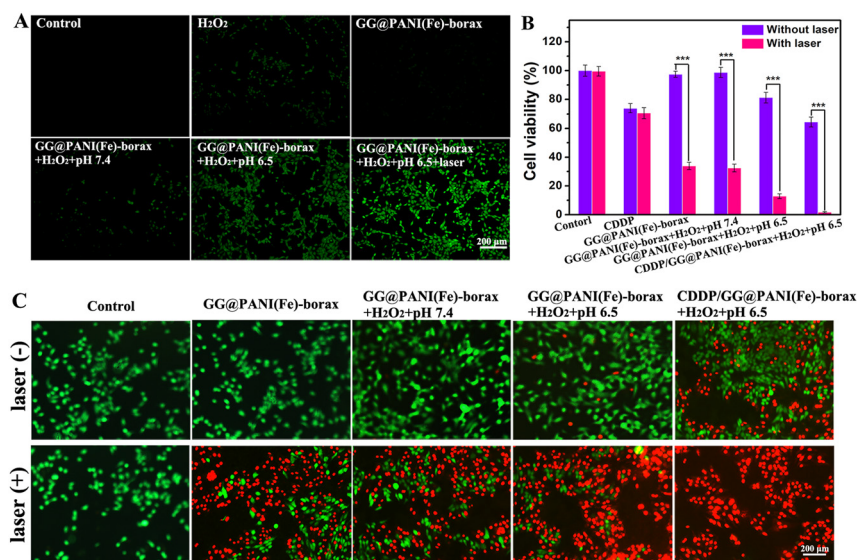

Fig. 6 *In vitro* cell-killing efficiency assay. (A) Intracellular $^{\bullet}OH$ generation in B16 cell detection with DCFH-DA after different treatments. (B) Relative cell viability of B16 cells after receiving different treatments ($n = 5$, ***$P < 0.001$), and (C) the corresponding live/dead staining images co-stained with Calcein AM (green) and PI (red).
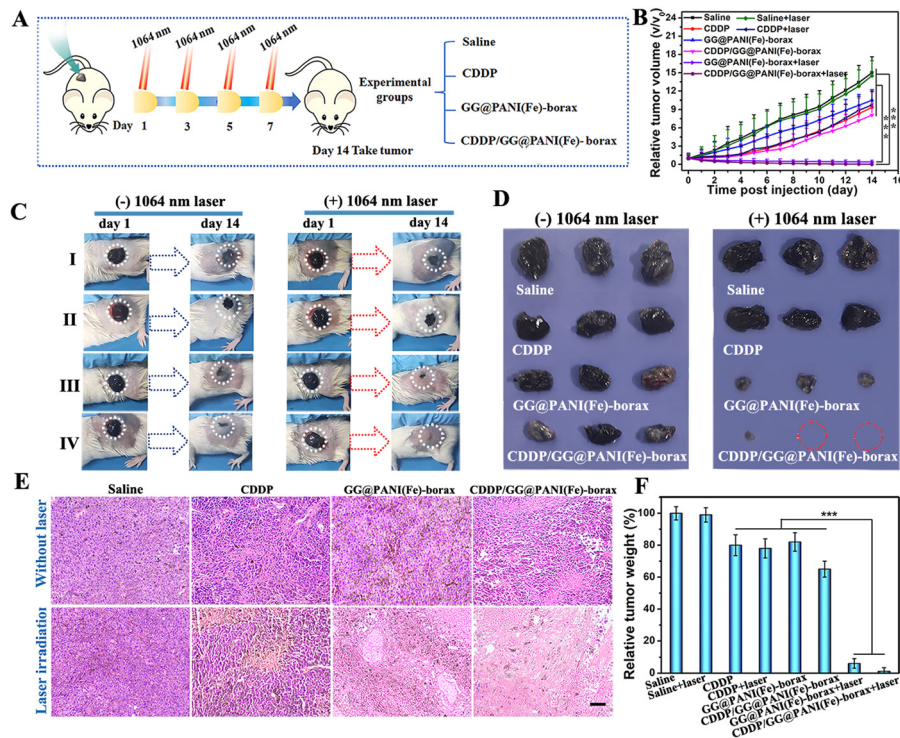
Fig. 7 The evaluation of *in vivo* anti-cancer efficacy. (A) Schematic diagram of the melanoma therapeutic procedure. (B) Time-dependent tumor growth curves over the treatment period ($n = 3$, ***$P < 0.001$). (C) Representative photographs of tumor-bearing mice before and after the treatments for each group (I: saline group, II: CDDP group, III: GG@PANI(Fe)-borax group, IV: CDDP/GG@PANI(Fe)-borax group). (D) Digital photos of resected tumors obtained at the end of the experiment. (E) H&E staining of the tumor sections (scale bars, 100 µm). (F) The relative tumor weight of resected tumors at the end of the treatment in different treatment groups.

borax or CDDP/GG@PANI(Fe)-borax) exhibited an NIR-II induced tumor-site temperature rise to 49.5 °C and 49.7 °C, respectively (Fig. S26, ESI†). These temperatures were high enough for both photothermal killing of cancer cells and triggering of the gel-to-sol conversion to release CDDP for synergic therapy. Moreover, the maximum temperature remained above 47.5 °C with negligible regression during the following three laser-treatments (Fig. S27, ESI†). Contrarily, the tumor temperature was only slightly elevated in the saline control and free CDDP groups due to the lack of photothermal components.

To assess the antitumor efficiency *in vivo*, the tumor size and body weight of B16 tumor-bearing mice were recorded daily. As observed in Fig. 7B, the tumor growth of mice treated with GG@PANI(Fe)-borax hydrogel exhibited relatively slow and slight inhibition compared with the mice treated with saline, which could be attributed to the production of toxic •OH *via* GG@PANI(Fe)-borax-mediated Fenton reaction under the specific H_2O_2-enriched TME. In comparison, the tumor treated with the GG@PANI(Fe)-borax hydrogel followed by laser irradiation displayed remarkably enhanced inhibition with negligible tumor growth, and the skin wound was almost healed after 14 days of treatment, which is mainly contributed to the combination of the NIR-II laser induced hyperthermia effect of the GG@PANI(Fe)-borax hydrogel and the photothermal-enhanced •OH generation, which can efficiently mediate the killing of cancer cells. The excellent wound healing effect

revealed that the iron ion-doped GG@PANI(Fe)-borax hydrogel could not only treat skin tumors through synergistic PTT and CDT, but can also promote subsequent skin wound healing (Fig. 7C). Notably, the mice receiving the CDDP/GG@PANI(Fe)-borax hydrogel plus laser exhibited the best tumor ablation, and some of the tumors were complete eradicated, which was ascribed to the superior synergistic effects of PTT-CDT and NIR-triggered CDDP delivery (Fig. 7D). Moreover, the histopathological analysis of the tumor sections in both the GG@PANI(Fe)-borax + laser and CDDP/GG@PANI(Fe)-borax + laser groups exhibited extensive apoptosis and necrosis, and in particular almost no intact tumor cells were visible in the CDDP/GG@PANI(Fe)-borax+ laser group (Fig. 7E), substantiating the significant anti-tumor effect of the multifunctional hydrogel for NIR-II laser mediated synergic PTT-CDT and chemotherapy. The resultant tumor inhibition rate in the CDDP/GG@PANI(Fe)-borax + laser group reached 98.8% according to the relative weight of the excised tumor at the end of the treatments (Fig. 7F).

Besides, the mice in the free CDDP group exhibited slight body weight loss and mild nephrotoxicity with the partial disappearance of renal capsule cavity due to the toxicity of CDDP, while no apparent body weight loss and no detectable lesions in major organs (including kidney) neither in the CDDP/GG@PANI(Fe)-borax group nor in the single GG@PANI(Fe)-borax hydrogel group (Fig. S28 and S29, ESI†). Meanwhile, the biodistribution of CDDP indicated that the GG@PANI(Fe)-

This journal is © The Royal Society of Chemistry 2022

J. Mater. Chem. B, 2022, **10**, 7717–7731 | **7727**

borax hydrogel could maintain a higher CDDP accumulation rate in tumor, effectively avoiding its nonspecific distribution (Fig. S30, ESI†). The above results demonstrated that the present hydrogel platform had satisfactory biosafety and was capable of eliminating the CDDP-related side effects by encapsulating CDDP in its porous network.

Antibacterial activity evaluation *in vitro*

Bacterial invasion remains a critical challenge during or after cutaneous cancer therapy, and a tumor-initiated skin defect can lead to chronic wound or other lethal complications, the antibacterial activity of the hydrogel can effectively avoid the possible infection during cutaneous cancer treatment and be beneficial for wound healing. The antibacterial performance of the prepared hydrogels against Gram-negative *E. coli* and Gram-positive *S. aureus* was evaluated; these bacteria are responsible for most infections. As displayed in the spread plate images of Fig. 8A and B, a slight reduction of colony numbers for both *E. coli* and *S. aureus* was observed in the GG-borax group compared to the control group due to the presence of antibacterial borax. In contrast, the number of *E. coli* and *S. aureus* colonies decreased remarkably in the GG@PANI-borax group, especially for *S. aureus*, which could be ascribed to the intrinsic antibacterial property of the PANI component, and the distinct bactericidal effect against *S. aureus* may result from the specific interaction of PANI with lipoteichoic acid molecules in the cell walls of Gram-positive bacteria.[54] More importantly, only very

few *E. coli* and almost no *S. aureus* left could be seen after co-culturing with the GG@PANI(Fe)-borax hydrogel, and the antibacterial efficiency of the GG@PANI(Fe)-borax hydrogel was almost up to 100% against both *E. coli* and *S. aureus*. This excellent antibacterial activity is mainly assigned to the combined effect of the intrinsic antibiotic activity of PANI and iron ions.[55] The above results revealed that our hydrogel as a promising integrated platform can not only effectively induce cancerous cell death, but also possesses superior antimicrobial activity, which is expected to accelerate infected-wound healing.

In vivo antibacterial and infected-wound healing

Encouraged by the *in vitro* achievements, the potential of the prepared hydrogel for bacteria inhibition and infected wound healing *in vivo* was further estimated using an *S. aureus*-infected full-thickness skin wound model. Typically, a full-thickness skin incision was created and *S. aureus* solution (1.5×10^6 CFU mL^{-1}) was introduced onto the wound. Thereafter, the infected wound defects were dressed with *in situ* injected hydrogels including GG-borax, GG@PANI-borax and GG@PANI(Fe)-borax, respectively (Fig. S31, ESI†). This injection process is shown in Video S1 in the ESI.† To determine the residual bacteria at the infected sites, tissues from the skin wounds were collected at day 12. As shown in the spread plate images of Fig. 9A, there was almost no residual bacteria in the GG@PANI (Fe)-borax group, and its relative bacterial viability was as low as 0.2%, which was significantly lower than those in the GG-borax group (84.8%) and GG@PANI-borax group (37.9%) (Fig. 9B). These results revealed that GG@PANI(Fe)-borax could effectively eradicate *S. aureus* bacterial infection.

In addition, the wound areas of the mice were tracked photographically during the treatment process, and the changes of wound size in 12 days are shown in Fig. 9C-E, on day 3 post treatment, the wound area in GG@PANI(Fe)-borax and GG@PANI-borax group was obviously smaller than those in the GG-borax or untreated control groups, and it could be seen that there were obvious abscesses at the sites of infected wounds in the untreated control, which hindered the skin repair. Notably, the wound treated with GG@PANI(Fe)-borax hydrogel was almost completely healed and the hair regrew on the original wound site after 12 days of treatment, and the ultimate wound closure rate was determined to be 99.8%, which was significantly higher than the other three groups, revealing the promising wound healing effect of the GG@PANI(Fe)-borax hydrogel.

Furthermore, the wound after 12 days of treatment was analyzed by H&E staining, as displayed in Fig. 9F, and the wound tissues in the three groups treated with hydrogels were all covered with neonatal epidermis or dermal tissue layers, but abundant regenerated hair follicles (green arrows) and new blood vessels (blue arrows) appeared only in the GG@PANI(Fe)-borax hydrogel group. This promising wound healing effect could be attributed to the bioactive iron ions contained in the GG@PANI(Fe)-borax, which not only significantly enhanced the antibacterial effect, but also promoted the proliferation of
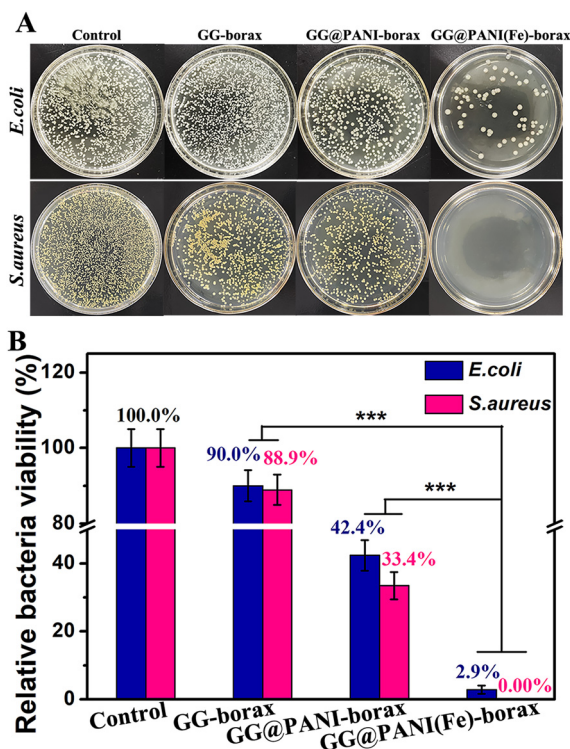

Fig. 8 Antibacterial activity *in vitro*. (A) Photographs of *E. coli* and *S. aureus* colonies after treatments with GG-borax, GG@PANI-borax and GG@PANI(Fe)-borax *in vitro* and (B) the corresponding relative bacteria survival rates of *E. coli* and *S. aureus*.
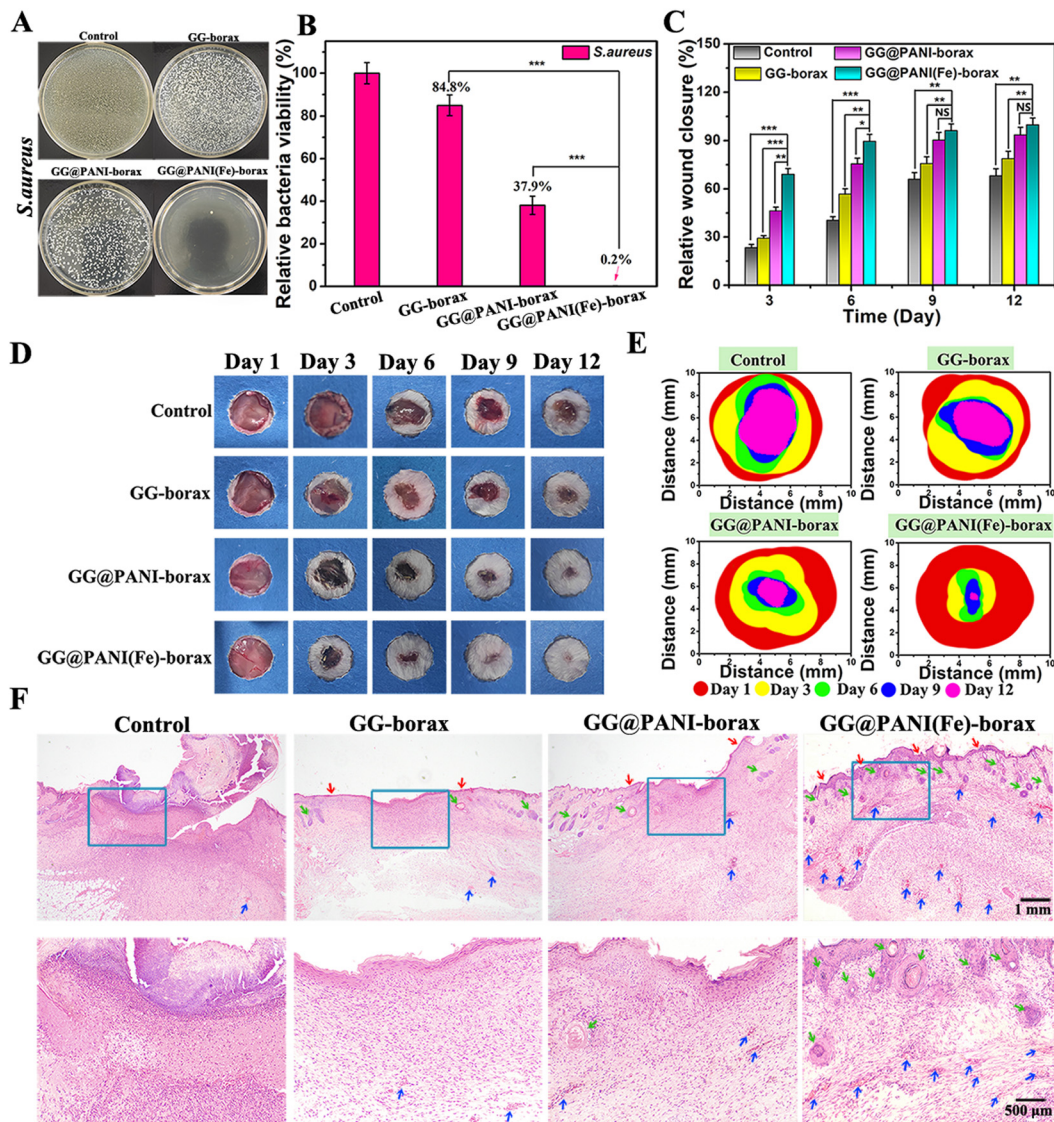
7728 | *J. Mater. Chem. B*, 2022, **10**, 7717–7731

This journal is © The Royal Society of Chemistry 2022

Fig. 9 Antibacterial activity and accelerated infected wound healing ability *in vivo*. (A) The spread plate photographs of residual *S. aureus* from infected wound sites at day 12, and (B) the corresponding relative bacteria survival rates of *S. aureus*. (C) *In vivo* wound healing ratio among different groups at different time points over 12 days (n = 3, *p < 0.05, **p < 0.01, ***p < 0.001, NS = no significant difference). (D) The representative photographs of the *S. aureus*-infected wound healing process. (E) Schematic diagram of the changes in wound-wed morphology during 12 days for each treatment. (F) H&E staining of skin wound tissues at day 12. Red arrows: neonatal epidermis; Green arrow: hair follicles and sebaceous glands; Blue arrow: new blood vessels.

fibroblast cells and revascularization, resulting in the acceleration of wound repair and skin tissue reestablishment.[51]

Conclusions

In conclusion, a facile approach was successfully developed to fabricate an "all-in-one" multifunctional hydrogel, which was based on a GG modified conjugated polymer doped with iron ions (GG@PANI(Fe)) and borax crosslinked by dynamic covalent borate/didiol linkages and hydrogen bonding. This multifunctional hydrogel displayed satisfied injectability, rapid self-healing properties, thermal- and pH-responsive gel–sol transition, and the desired biocompatibility for antitumor application. The GG@PANI(Fe) composites in the network

endowed the hydrogel with excellent NIR-II-mediated photothermal performance and Fenton reaction-induced •OH production ability, with multiple therapeutic capabilities for the eradication of cancerous cells. In addition, iron ion-doped PANI also provided the hydrogel with favorable antimicrobial activity for elimination of wound infection during or after skin tumor treatment. Furthermore, the bioactive iron ions contained in the hydrogel can promote proliferation of fibroblast cells and revascularization for expediting tumor-initiated wound healing. Taken together, this work presented a facile strategy to fabricate injectable, self-healing multi-functional hydrogels as potential promising materials for skin tumor therapy with simultaneous tumor eradication, bacterial inhibition, and skin wound healing acceleration.

This journal is © The Royal Society of Chemistry 2022

J. Mater. Chem. B, 2022, **10**, 7717–7731 | **7729**

Conflicts of interest

The authors declare that they have no known competing financial interests or personal relationships that could have appeared to influence the work reported in this paper.

Acknowledgements

Notes and references

1 G. C. Leonardi, L. Falzone, R. Salemi, A. Zanghì, D. A. Spandidos, J. A. Mccubrey, S. Candido and M. Libra, *Int. J. Oncol.*, 2018, **52**, 1071–1080.

2 J. Xie, R. J. Liang, Q. R. Li, K. Wang, M. Hussain, L. Y. Dong, C. Shen, H. L. Li, G. X. Shen, J. T. Zhu and J. Tao, *Acta Biomater.*, 2022, **142**, 264–273.

3 W. D. Wang, C. Chen, Y. Ying, S. R. Lv, Y. Wang, X. Zhang, Z. H. Cai, W. X. Gu, Z. Li, G. Jiang and F. L. Gao, *ACS Nano*, 2022, **16**, 5597–5614.

4 H. S. Ma, Q. Zhou, J. Chang and C. T. Wu, *ACS Nano*, 2019, **13**, 4302–4311.

5 D. F. Zhi, T. Yang, J. O'Hagan, S. B. Zhang and R. F. Donnelly, *J. Controlled Release*, 2020, **325**, 52–71.

6 J. W. Zhao, Q. Zhang, W. Q. Liu, G. Y. Shan and X. Wang, *Colloids Surf., B*, 2022, **211**, 112295.

7 Z. Li, Y. H. Yang, J. R. Yao, Z. Z. Shao and X. Chen, *Mater. Sci. Eng., C*, 2017, **79**, 123–129.

8 Y. G. Zhang, S. Y. Zhang, Z. H. Zhang, L. L. Ji, J. M. Zhang, Q. H. Wang, T. Guo, S. Ni, R. Cai, X. Y. Mu, W. Long and H. Wang, *Front. Chem.*, 2021, **9**, 728066.

9 Z. Y. Jiang, C. L. Zhang, X. Q. Wang, M. Yan, Z. X. Ling, Y. C. Chen and Z. P. Liu, *Angew. Chem., Int. Ed.*, 2021, **60**, 22376–22384.

10 Y. Chen, P. Y. He, D. Jana, D. D. Wang, M. H. Wang, P. Y. Yu, W. Zhu and Y. L. Zhao, *Adv. Mater.*, 2022, 2201706.

11 J. J. Fu, J. Y. Zhang, S. P. Li, L. M. Zhang, Z. X. Lin, L. Liang, A. P. Qin and X. Y. Yu, *Mol. Pharmaceutics*, 2018, **15**, 4621–4631.

12 J. D. Xia, X. Q. Qing, J. J. Shen, M. B. Ding, Y. Wang, N. Y. Yu, J. C. Li and X. H. Wang, *Front. Chem.*, 2021, **9**, 736468.

13 B. Liu, J. Sun, J. J. Zhu, B. Li, C. Ma, X. Q. Gu, K. Liu, H. J. Zhang, F. Wang, J. J. Su and Y. Yang, *Adv. Mater.*, 2020, **32**, 2004460.

14 S. Q. Wang, H. Zheng, L. Zhou, F. Cheng, Z. Liu, H. P. Zhang and Q. Y. Zhang, *Biomaterials*, 2020, **260**, 120314.

15 S. Y. Wang, B. H. Chen, L. P. Ouyang, D. H. Wang, J. Tan, Y. Q. Qiao, S. F. Ge, J. Ruan, A. Zhuang, X. Y. Liu and R. B. Jia, *Adv. Sci.*, 2021, **8**, 2004721.

16 Y. Miao, Jiawei Lu, Junhui Yin, C. Zhou, Y. Guo and S. Zhou, *Nanotechnol. Rev.*, 2019, **8**, 645–660.

17 Y. Y. Liu, Y. X. Xi, J. L. Zhao, J. Y. Zhao, J. C. Li, G. Q. Huang, J. Q. Li, F. Fang, L. L. Gu and S. G. Wang, *Chem. Eng. J.*, 2019, **375**, 122048.

18 Y. X. Yang, X. D. Zhao, J. Yu, X. X. Chen, R. Y. Wang, M. Y. Zhang, Q. Zhang, Y. F. Zhang, S. Wang and Y. L. Cheng, *Bioact. Mater.*, 2021, **6**, 3962–3975.

19 G. Gao, Y. W. Jiang, H. R. Jia and F. G. Wu, *Biomaterials*, 2019, **188**, 83–95.

20 S. J. Yu, S. Wei, L. Liu, D. S. Qi, J. Y. Wang, G. J. Chen, W. Y. He, C. L. He, X. S. Chen and Z. Gu, *Biomater. Sci.*, 2019, **7**, 860–866.

21 C. J. Liu, X. L. Guo, C. P. Ruan, H. L. Hu, B. P. Jiang, H. Liang and X. C. Shen, *Acta Biomater.*, 2019, **96**, 281–294.

22 C. J. Liu, C. P. Ruan, R. Shi, B. P. Jiang, S. J. Ji and X. C. Shen, *Biomater. Sci.*, 2019, **7**, 1705–1715.

23 A. H. Pandit, N. Mazumdar and S. Ahmad, *Int. J. Biol. Macromol.*, 2019, **137**, 853–869.

24 P. F. Sun, T. Huang, X. X. Wang, G. N. Wang, Z. J. Liu, G. S. Chen and Q. L. Fan, *Biomacromolecules*, 2020, **21**, 556–565.

25 C. C. Ding, Q. L. Yang, M. D. Tian, C. C. Guo, F. Deng, Y. Dang and M. Zhang, *Polym. Int.*, 2020, **69**, 858–866.

26 H. An, Y. Yang, Z. W. Zhou, Y. Y. Bo, Y. Wang, Y. N. He, D. Wang and J. L. Qin, *Acta Biomater.*, 2021, **131**, 149–161.

27 J. Yang, J. Choi, D. Bang, E. Kim, E. K. Lim, H. Park, J. S. Suh, K. Lee, K. H. Yoo, E. K. Kim, Y. M. Huh and S. Haam, *Angew. Chem., Int. Ed.*, 2011, **50**, 441–444.

28 Q. W. Tian, Y. P. Li, S. S. Jiang, L. An, J. M. Lin, H. X. Wu, P. Huang and S. P. Yang, *Small*, 2019, **15**, 1902926.

29 S. L. Wang, L. L. Zhang, J. J. Zhao, M. He, Y. Huang and S. L. Zhao, *Sci. Adv.*, 2021, **7**, eabe3588.

30 B. Getiren, Z. Çıplak, C. Gökalp and N. Yıldız, *J. Appl. Polym. Sci.*, 2020, **137**, e49343.

31 S. N. Geng, H. Zhao, G. T. Zhan, Y. B. Zhao and X. L. Yang, *ACS Appl. Mater. Interfaces*, 2020, **12**, 7995–8005.

32 S. R. Zhou, C. G. Yang, L. X. Guo, Y. X. Wang, G. F. Zhang and L. H. Feng, *Chem. Commun.*, 2019, **55**, 8615–8618.

33 A. N. Andriianova, L. R. Latypova, L. Y. Vasilova, S. V. Kiseleva, V. V. Zorin, I. B. Abdrakhmanov and A. G. Mustafin, *J. Appl. Polym. Sci.*, 2021, **138**, e51397.

34 P. Boomi, G. P. Poorani, S. Palanisamy, S. Selvam, G. Ramanathan, S. Ravikumar, H. Barabadi, H. G. Prabu, J. Jeyakanthan and M. Saravanan, *J. Cluster Sci.*, 2019, **30**, 715–726.

35 R. S. Diggikar, S. P. Deshmukh, T. S. Thopate and S. R. Kshirsagar, *ACS Omega*, 2019, **4**, 5741–5749.

36 L. P. Wang, R. J. Vivek, W. F. Wu, G. W. Wang and J. Y. Wang, *ACS Biomater. Sci. Eng.*, 2018, **4**, 1880–1890.

37 Y. Hong, W. Cho, J. Kim, S. Hwng, E. Lee, D. Heo, M. Ku, J. S. Suh, J. Yang and J. H. Kim, *Nanotechnology*, 2016, **27**, 185104.

38 E. Ju, K. Dong, Z. Liu, F. Pu, J. S. Ren and X. G. Qu, *Adv. Funct. Mater.*, 2015, **25**, 1574–1580.

39 M. Lin, D. D. Wang, S. Y. Li, Q. Tang, S. W. Liu, R. Ge, Y. Liu, D. Q. Zhang, H. C. Sun, H. Zhang and B. Yang, *Biomaterials*, 2016, **104**, 213–222.

7730 | *J. Mater. Chem. B*, 2022, **10**, 7717–7731

This journal is © The Royal Society of Chemistry 2022

40 C. Korupalli, P. Kalluru, K. Nuthalapati, N. Kuthala, S. Thangudu and R. Vankayala, *Bioengineering*, 2020, **7**, 94.

41 N. Li, C. J. Liu and W. Chen, *J. Agric. Food Chem.*, 2019, **67**, 746–752.

42 C. Ma, H. W. Pang, H. G. Liu, Q. Yan, J. Z. Li and S. F. Zhang, *J. Mater. Chem. B*, 2021, **9**, 4230–4240.

43 C. Talodthaisong, W. Boonta, S. Thammawithan, R. Patramanon, N. Kamonsutthipaijit, J. A. Hutchison and S. Kulchat, *Mater. Today Commun.*, 2020, **24**, 100992.

44 A. P. Gupta and D. K. Verma, *J. Nanostruct. Chem.*, 2015, **5**, 405.

45 B. P. Jiang, L. Zhang, X. L. Guo, X. C. Shen, Y. Wang, Y. Zhu and H. Liang, *Small*, 2017, **13**, 1602496.

46 K. Dutta, B. Das, D. Mondal, A. Adhikari, D. Rana, A. K. Chattopadhyay, R. Banerjee, R. Mishra and D. Chattopadhyay, *New J. Chem.*, 2017, **41**, 9461–9471.

47 G. A. Alna'washi, A. M. Alsmadi, I. Bsoul, B. Salameh, G. M. Alzoubi, M. Shatnawi, S. M. Hamasha and S. H. Mahmood, *Results Phys.*, 2021, **28**, 104574.

48 T. Yamashita and P. Hayes, *Appl. Surf. Sci.*, 2008, **254**, 2441–2449.

49 C. Z. Jia, H. W. Liu, Y. X. Hu, H. Wu, C. P. Zhu, Y. X. Zhang, S. G. Wang and M. X. Huang, *ChemistrySelect*, 2021, **6**, 6564–6573.

50 Z. H. Miao, Y. B. Sun, Z. C. Tao, Y. Chen, Y. Ma, D. D. Zhu, X. Huang and Z. B. Zha, *Adv. Healthcare Mater.*, 2021, 2100722.

51 B. Marco-Dufort and M. W. Tibbitt, *Mater. Today Chem.*, 2019, **12**, 16–33.

52 C. Yin, X. Z. Li, Y. Wang, Y. Y. Liang, S. Zhou, P. C. Zhao, C. S. Lee, Q. L. Fan and W. Huang, *Adv. Funct. Mater.*, 2021, **31**, 2104650.

53 W. P. Ma, H. S. Ma, P. F. Qiu, H. J. Zhang, Z. B. Yang, B. Ma, J. Chang, X. Shi and C. T. Wu, *Biomaterials*, 2021, **279**, 121225.

54 H. F. Tang, Y. F. Liu, B. Li, B. Shang, J. C. Yang, C. R. Zhang, L. J. Yang, K. Z. Chen, W. Wang and J. F. Liu, *Bioact. Mater.*, 2021, **6**, 4758–4771.

55 M. S. Ma, Y. L. Zhong and X. L. Jiang, *J. Mater. Chem. B*, 2021, **9**, 4567–4576.

This journal is © The Royal Society of Chemistry 2022

J. Mater. Chem. B, 2022, **10**, 7717–7731 | 7731